Stress reduction effects of ultra-high performance fiber reinforced concrete overlaid steel bridge deck developed with a new interfacial bond method

Pengru Deng[1*], Hongji Mi[2], Hiroshi Mitamura[3] and Takashi Matsumoto[4]

[1]Assistant Professor, Faculty of Engineering, Hokkaido University, Hokkaido 060-8628, Japan; Email: pengrudeng@eng.hokudai.ac.jp
[2]Researcher, China Nuclear Mining Science and Technology Corporation, Shijiazhuang 050021, China; Email: miyuki950404@yahoo.com
[3]Researcher, The Calamity Science Institute, Osaka 541-0043, Japan; mitamura@sunbridge.jp
[4]Professor, Faculty of Engineering, Hokkaido University, Hokkaido 060-8628, Japan; Email: takashim@eng.kokudai.ac.jp
[*]Corresponding author

ABSTRACT

The effects of a 25 mm of UHPFRC overlay on reducing the stress of the open ribs-stiffened orthotropic steel decks (OSDs) are assessed experimentally and analytically. To integrate the UHPFRC overlay and the OSDs, an adhesive-based bonding technique is developed and evaluated beforehand using a pull-off test and a three-point bending test, where a 3 MPa of excellent bond strength and an invisible slip demonstrate the reliability of the technique. With the developed bonding technique, an up to 80% of strain reduction and a peak clipping phenomenon are observed in the strain of the critical locations of the steel deck and structural members in the hotspot areas due to the UHPFRC. In addition, it is found that the superior high strengths and the strain-hardening of UHPFRC can postpone the initiation and propagation of cracks. As a result, an effective enhancement of stiffness of OSDs and an apparent fatigue life extension can be achieved even with a thin layer.

KEYWORDS

UHPFRC; steel bridge deck; interfacial bond; stress reduction; FEM

1 INTRODUCTION

Taking advantage of the excellent characteristics, such as high load capacity/weight ratio, durability, and expedient constructability, orthotropic steel decks (OSDs) have been widely employed in bridge structures, especially long-span bridges [1]. Compared to the OSDs stiffened with closed ribs, the OSDs stiffened with open ribs exhibited better fatigue performance as local secondary stress which is caused by a partial restraint of the closed ribs at the unconfined bottom floor beams is eliminated in the open ribs [2]. However, recently, fatigue cracks were still observed in orthotropic steel bridge decks with open ribs like bulb ribs in Japan, which was mainly attributed to the increasing heavy-loaded vehicles together with the attacks of corrosions that intruded through the pavement. It was reported that the corroded thickness may reach up to tens of percent of the design thickness of the deck [3]. Therefore, it is of great significance to develop effective rehabilitation techniques, which may both improve mechanical capabilities and prevent the corrosion elements, to improve the performance and durability of the OSDs with open.

According to the existing studies, it was verified that overlaying cementitious materials, such as plain concrete, reinforced concrete (RC), steel fiber reinforced concrete (SFRC), and engineering cementitious composites (ECC), with a thickness of about 50 mm can effectively reduce the stresses in the OSDs of existing bridges, and hence improve the fatigue performance [4-6]. These studies also suggested that the

effectiveness of the improvement depends greatly on the strengths and ductility of the overlaid material. Therefore, an innovative composite, i.e. ultra-high performance fiber reinforced concrete (UHPFRC), should be a suitable and appropriate option for the overlaid material as it has superior mechanical properties in addition to a very low penetrability [7-11]. These two aspects of characteristics of UHPFRC are perfectly matched to the introduced two requirements of a rehabilitation technique of the deteriorated OSDs with open ribs. On one hand, owing to the extraordinarily high mechanical strengths (>130 MPa in compression and >8 MPa in tension) and a strain hardening behavior of UHPFRC, a remarkable increase of load capacities and decrease of stress levels of the bridge OSDs can be achieved by the overlaid UHPFRC even with a relatively small thickness. Besides, the application of the thin UHPFRC overlays creates a negligible increase of self-weight. On the other hand, as UHPFRC is a high density, homogenous, and specifically tailored cementitious-based composite, the permeability of it is extremely low especially for the intact uncracked UHPFRC. Hence, the overlaid UHPFRC can almost cut off the corrosion elements from the upper surface.

In terms of strengthening the OSDs using a UHPFRC overlay, the connection between the substrate steel decks and the UHPFRC overlay must have sufficient rigidity and strength in order to ensure the designed composite behavior of the composite decks. Adhesive bond and headed studs were the two options in the existing applications to realize this connection [12, 13]. Even though the most commonly employed option was the mechanical metal shear studs, some defects have been widely observed, such as the fatigue problems induced by welding the studs on the existing steel decks and the cracking of the overlaid cementitious composites around the studs due to a stress concentration [14-16]. Besides, the adhesive bond may be the even more appropriate option specifically for the UHPFRC-steel connection based on the following considerations. Firstly, the high rigidity provided by adhesive bond can facilitate a full utilization of the high strengths of UHPFRC [4, 17-19]. Moreover, if the steel studs are employed instead, the live load-induced stress may not be effectively redistributed to the UHPFRC to generate a high but appropriate stress level even though a high level of local stress may be generated in areas adjacent to the steel studs. Accordingly, the stress reduction effects of using UHPFRC may not so different from using materials with lower strengths like plain concrete or ECC. Secondly, the studs must be placed in a high density to have a similar and sufficient rigidity. These densely placed connectors may furtherly lead to many fatigue and construction problems. Last but not the least, in the existing applications of strengthening bridge decks with a UHPFRC overlay, a 20-25 mm thickness was validated to be capable of affording a considerable enhancement of structural strength and stiffness, and thereby normally employed to minimize the extra self-weight. Obviously, this thin layer is not enough for setting the studs. Therefore, in the scale of the adhesive bond, this study primarily proposed a bonding technique for the UHPFRC-steel interface based on the results of a pull-off test and a three-point bending test of the UHPFRC-steel composite with a series of bonding techniques using different bonding agents, and interface treatments. The test results demonstrated that the technique can provide sufficient rigidity, strength and compatibility. Moreover, using the identified bonding technique, a rehabilitation technique for an open ribs-stiffened orthotropic bridge deck by overlaying UHPFRC was developed and then accessed experimentally as well as analytically based on a nonlinear finite element method, where the post-cracking characteristics of UHPFRC including the strain-hardening and softening behaviors were included. Attributing to the UHPFRC overlay, an apparent stress reduction effect was exhibited, especially at the critical locations of the steel deck and the transverse crossbeams like the hotspot areas. As the fatigue life of steel members is directly dependent on the stress amplitude, the reduced stress level indicated the effectiveness of the overlaid UHPFRC. Besides, as the cracking initiation and propagation in UHPFRC may be postponed and decelerated by the superior high strength and the strain-hardening of UHPFRC, respectively, the additional stiffness provided by the UHPFRC overlay did not exhibit dramatically

decrease after cracking. As a result, an effective enhancement of stiffness of the OSDs could be provided by even a thin layer of UHPFRC. Furthermore, a fatigue life prediction of the OSDs was implemented focusing on the critical locations, where the OSD could service for over 100 years after overlaying the UHPFRC.

2 DEVELOPMENT OF A NEW INTERFACIAL BOND

The bonding method using adhesive was developed primarily in steel-concrete composite structures in the 1960s [20] and then exploited in connecting steel and other cementitious composites including ultra-high performance concrete (UHPC). Normally, the performance of the bond interface was characterized in both the tangential and normal directions exploiting methods such as push-out test, pull-off test, and flexural test [17, 18]. It was demonstrated that the adhesive the adhesive-based bond connection could ensure a much higher level of integrity of the composite structure as it could provide a continuous transmission of the shear force [21]. Therefore, in this study, the adhesive-based bonding techniques are evaluated along the normal direction exploiting the strengths from a pull-off tensile test [22, 23]. As for the compatibility along the tangential direction, it is assessed complementarily by the flexural behaviors of UHPFRC-steel plate composite beams.

2.1 Investigation along the interface normal direction

2.1.1 Pull-off tensile test

In this study, the pull-off test was conducted with an apparatus typed as LPT-1500 as shown in **Fig. 1**. The load was applied on the core specimens of square section with dimensions 20×20 mm. The load capacity of LPT-1500 is 15 kN which is considered to be sufficient for this test as it can create tensile stress much higher than the tensile strength of a typical UHPFRC.

As shown in **Fig. 1**, the load can be applied through the pull pin supported by a reaction frame. It was reported that the key of a pull-off test is to ensure that the applied tensile force is normally applied to the targeted surface [24]. The testing apparatus was set up and aligned carefully after the hardening of the adhesive as follows and as shown in **Fig. 1**. Step 1: a couple of parallel lines were drawn beforehand on two opposite sides of each attachment at a distance equal to half of the distance between the two legs of the apparatus; Step 2: plaster bags and flat iron sheets were placed under the feet of the ram chair of the apparatus; Step 3: connecting the loading apparatus with the attached base by fastening the screw between them; Step 4: assembling and confirming all the other components of the apparatus. It was expected that a direct tensile loading could be realized with high accuracy following this process. After alignment, the uniaxial tensile force was then gradually applied to the pull pin as smoothly and continuously as possible until final failure, where one could obtain the ultimate load capacity of the specimens. The pull-off strength (S_{PO}) was then calculated by dividing load capacity (F_T) by the measured area of the fracture surface (A_f).

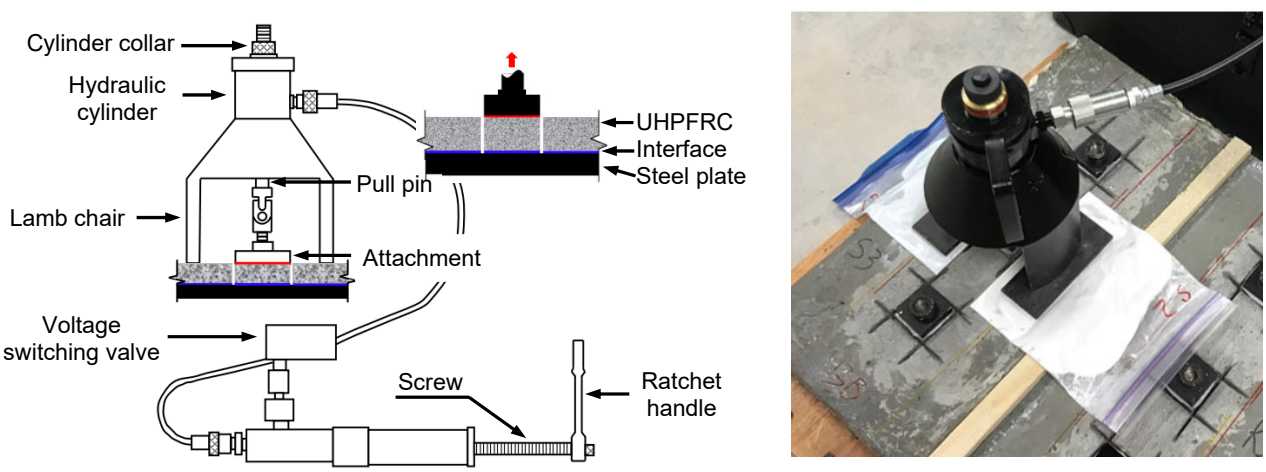

(a) Schematical diagram (b) Image of test

Fig. 1 Set up of pull-off test

2.1.2 Bond adhesives and interface treatments

To develop an appropriate bonding technique, the performance of three different bonding adhesives named KS bond, Smart bond, and E250 was investigated firstly as shown in **Fig. 2(a)**. KS bond is a kind of bonding agent normally used in combining the cast-in-place (fresh) concrete to the substrate concrete or steel with high durability. It affords high durability and a short construction period. Smart bond is a kind of epoxy bonding agent used in the joining part of concrete having rather high durability to water. The merit of the Smart bond is that it is applicable for the saturated substrate RC/steel surface. Besides, an early strength can be obtained by using the Smart bond. Bond adhesive E250 is characterized by its outstanding resistance to water, environmental attacks, and corrosion elements. The Bond E250 can also be used in wet conditions. The thickness of the bonding agent was about 2 mm and the specimens were prepared following the procedure shown in **Fig. 3**, where the used UHPFRC was composed of steel fibers, steel wool, water together with cement and a mixture which were specifically produced [25] as shown in **Fig. 4**. The length of the steel fiber was 13 mm and 0.16 mm, respectively. The steel fiber volume fraction was 4% and the water-to-cement ratio was 0.2. This UHPFRC was cast-in-place and used in the experiments in the entire study.

Except for the bonding adhesive, the bond properties and performance can be improved by changing the condition of the surface characteristics including interface roughness and moisture conditions prior to the application of the repair material [26]. In terms of the interface roughness, it was reported that a substrate roughening may improve overlay bond strength owing to a promoted interlock [27] as well as eliminate a weak or delamination of the overlaid material without introducing microcracks [26, 28]. Unlike the surface roughness, the effect of the moisture condition of the substrate remains controversial [26, 29, 30]. If the overlay cementitious material has a sufficiently high water-to-cement ratio (w/c $\geq$ 0.42) to ensure approximately full hydration [31, 32], the free water that moves from the pre-wetted surface of the substrate to the overlay material may increase the w/c ratio of the repair material resulting in a thin weak layer just above the interface. On the other hand, if there is a large amount of unhydrated cement in the repaired materials due to a low w/c ratio, a dry substrate surface may deprive the water of the repaired materials leading to a mostly unhydrated weak layer at the interface. Besides, the interface stress due to shrinkage may be reduced or eliminated by prewetting the interface [30, 33]. Obviously, the UHPFRC which normally possesses an ultra-low w/c ratio (0.14-0.19) belongs into the second category [34-36].

Thus, this study investigated the bonding conditions treated by adding aggregates as shown in **Fig. 2**. In E specimens, only bond E250 was used in the interface. In the ENE specimens, the aggregates were put inside the bond E250. In the ENW specimens, the elements under the UHPFRC were arranged in a sequence of aggregates, bond E250, and steel plate. In addition, water was sprayed on the aggregates before casting UHFPRC.

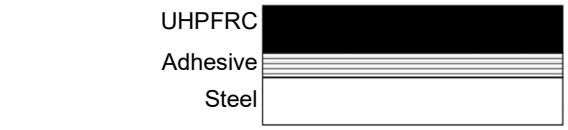

(a) E

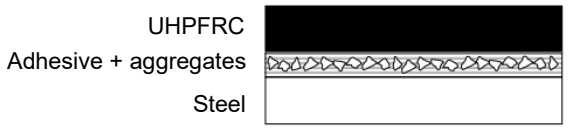

(b) ENE

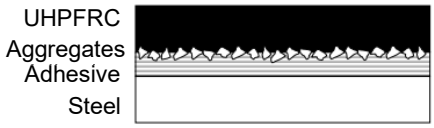

(c) ENW

Fig. 2 Interface treatment

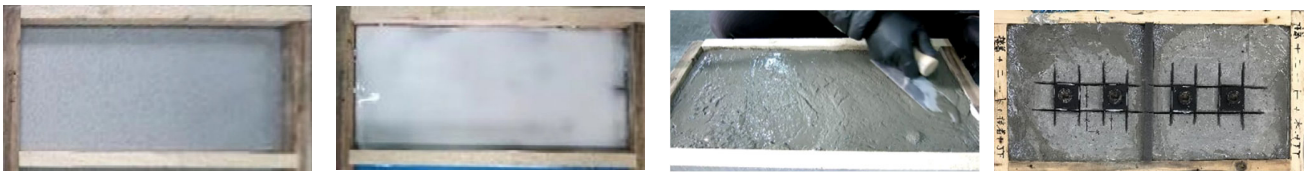

(a) Polishing steel plate (b) Interface treatment (c) Pour & Cast UHPFRC (d) Cut & set attachment

Fig. 3 Specimen preparation procedure

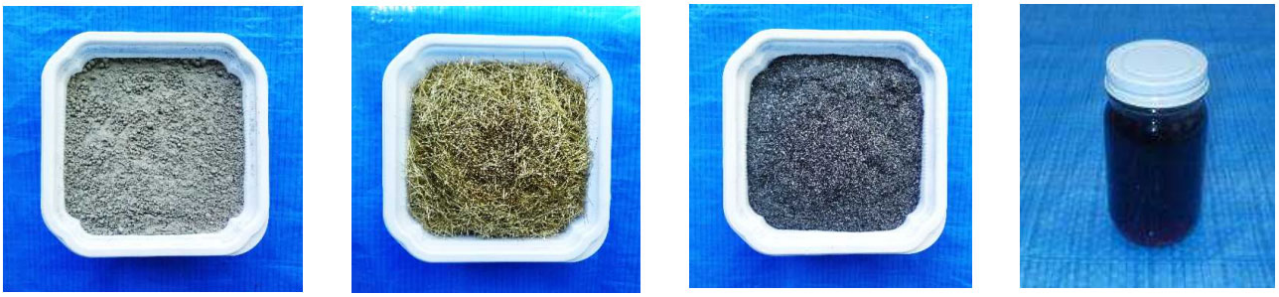

(a) Cement (b) Steel fiber (c) Steel wool (d) Mixture

Fig. 4 Specimen preparation procedure [25]

2.1.3 Results of pull-off test

The bond strength and fracture pattern after the pull-off test are listed in **Table 1** and **Table 2**, respectively, for specimens with the employed three bond adhesives and bond interface treatments. For different bond adhesives, it is found that the average bond strengths of specimens with Smart bond, KS bond, and E250 were 0.60 MPa, 0.51 MPa, and 3.00 MPa, respectively. Even though the variation of the bond strength of

using E250 was more apparent than using the Smart bond and KS bond, the strengths of using E250 were much larger. According to a sorting criterion presented specifically for the pull-off tests by Sprinkel and Ozyildirim [37], the performance of using E250 may be classified into "Excellent", whereas the performance of the other two bonding adhesives may be classified into "Poor". Correspondingly, the interfaces of using the three bonding adhesives also exhibited different fracture patterns as shown in **Table 2**. It is found that basically almost all of the KS bond and Smart bond were sticking to the substrate side and can hardly be observed on the pull-off side, which indicates that these two adhesives are much more compatible with the steel above the UHPFRC. Nevertheless, the bonding adhesive can be observed on both the substrate and the pull-off sides in the cases of using E250. Quantitatively, the amount of adhesive stick on the substrate steel accounted for an approximate 20% of all the adhesive on both sides in the specimens of E1 and E2, whereas an approximate 70% in the specimen of E3. On average, a ratio of 3 to 2 was obtained between the portions of adhesive sticking on the substrate steel to that on the overlaid UHPFRC. Even if the ratio was not equal to 1 to 1, it may be stated that the E250 possesses a similar degree of compatibility with the steel as well as the UHPFRC. This behavior facilitates the realization of the capacity of the adhesive.

In terms of the specimens exploiting bond E250 but with different treatments, i.e. E, ENE, and ENW, the failure pattern were totally different among these three groups of specimens. For the ENE group of specimens, consistency was observed in the failure pattern. It is found that the failures always happened between UHPFRC and bond interface because large areas of bond E250 could be found on the substrate sides of the 3 specimens. In terms of the specimens ENW1 and ENW2, as the failure occurred in the UHPFRC to attachment interface, the exact values of the strength cannot be obtained. The loads at stops were employed to obtain the bond strength, which was calculated to be 2.92 MPa and 3.12 MPa for ENW1 and ENW2, respectively. Correspondingly, only specimen ENW3 may be used to investigate the failure pattern of the ENW group. It is found that bond E250 and aggregates were attached on both the pulled-off side and the substrate side. This phenomenon indicates that the brittleness of the interface failure may be reduced by using the aggregates.

In summary, from the pull-off tests of the specimens using different bond adhesives and different interface treatments, all the three bond techniques using bond E250 exhibited excellent strengths along the normal direction of the interface. Therefore, they are worthy to be assessed furtherly.

Table 1 Bond strength of different interface treatments

Interface treatment	Bond strength (MPa)			Average bond strength (MPa)	Standard deviation (MPa)	Grade
	No. 1 Specimen	No. 2 Specimen	No. 3 Specimen			
KS	0.222	0.626	0.667	0.505	0.246	Poor
Smart	0.468	0.401	0.918	0.596	0.281	Poor
E	2.607	2.796	3.602	3.002	0.529	Excellent
ENE	2.539	2.851	3.385	2.925	0.428	Excellent
ENW	2.920	3.120	2.588	2.876	0.269	Excellent

Table 2 Fracture pattern after pull-off tests

Interface treatment	No. 1 specimen		No. 2 specimen		No. 3 specimen	
	UHPFRC side	Steel side	UHPFRC side	Steel side	UHPFRC side	Steel side
KS			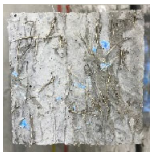			
Smart						
E	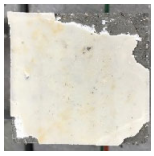		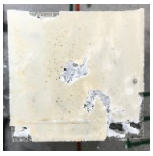			
ENE			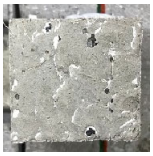		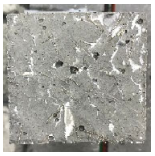	
ENW	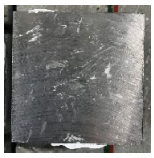		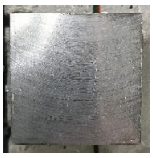		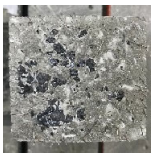	

2.2 Investigation along the interface tangential direction

2.2.1 Three-point bending test

Static three-point bending tests were further conducted on steel plate-UHPFRC composite beams investigating the performance of the interface treatment techniques along the tangential direction. The bonding techniques which were classified into "Excellent" based on the pull-off tests was employed for the steel plate-UHPFRC interface. In other words, the tested composite beams were integrated employing the interface treatments named E, ENE, and ENW. **Fig. 5** shows the configuration of the tested composite beams together with the loading and supporting configuration. The supporting span and the length attached with UHPFRC were 418 mm and 378 mm, respectively. The steel plate and UHPFRC had the same width of 50 mm. To be accurate, after detaching the specimens from wood plates, dimensions of every specimen were measured with vernier caliper. The UHPFRC was placed beneath the steel plate in the three-point bending tests to simulate the stress conditions of the negatively bended areas above the longitudinal stiffer. The thicknesses of steel plate and UHPFRC were 3 mm and 7 mm, respectively. The specimens were prepared following a procedure approximate to that show in **Fig. 3** except that "Cut & set attachment" was not conducted. The test was conducted under displacement-control at a rate of 2 mm/min until the final failure. For each specimen, two strain gauges were attached on the top surface of the steel plate at the two quarter points on both sides as shown in **Fig. 5**. The load was recorded directly from the loading machine.

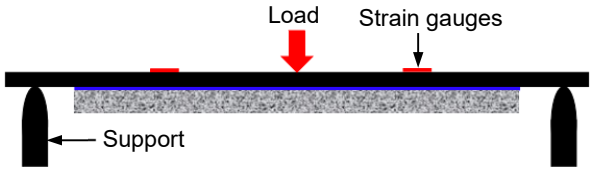

Fig. 5 Configuration of the three-point bending test

2.2.2 Structural mechanics-based analytical method

To evaluate the bonding condition indirectly, the tested composite beams were analyzed based on structural mechanics. A plane cross sectional assumption was employed for the steel-UHPFRC composite, which implicitly includes the perfect interface connection. According to this assumption, the strain along the depth direction should vary linearly as shown in **Fig. 6** and can be expressed as a function of the distance (t) of the concerned location away from the top surface.

$$\varepsilon_x(t) = \varepsilon_{cmax} - \frac{t}{t_m}\varepsilon_{cmax} \tag{1}$$

where t_m is the location of the neutral axis. ε_{cmax} is the compression strain of the steel fiber on the top surface. These are the two unknows in the sectional strain distribution equation. Hereafter, the sectional stress distribution can be obtained following the constitutive models of the materials.

In terms of the material characteristics of the composite beam, a perfect elastoplastic constitutive law was employed for the steel plate under both tension and compression (see. **Fig. 7(a)**). In this analysis, it was assumed that the failure occurs once the yield strength is reached. As for the UHFPRC, a stress-strain relation as shown in **Fig. 7(b)** was employed for the UHPFRC under compression. Under uniaxial tension, a trilinear constitutive model including the elastic, strain-hardening, and strain-softening domains was employed to represent the pre- and post-cracking behaviors of UHPFRC as shown in **Fig. 7(b)**. Correspondingly, the sectional stress distribution along the depth direction may be divided into four regions from top to bottom as shown in **Fig. 7**. The stress of the steel plate can be obtained by multiplying the elastic module with the strain, whereas the stress distribution of the UHPFRC may be expressed as:

$$\sigma_t(t) = \begin{cases} E_c\varepsilon_t & h_s < t \le h_s + h_u, \frac{f_{cr}}{E_c} \le \varepsilon_t \\ f_{cr} + E_h \cdot \left(\varepsilon_t - \frac{f_{cr}}{E_c}\right) & h_s < t \le h_s + h_u, \frac{f_{cr}}{E_c} + \frac{f_u - f_{cr}}{E_h} \le \varepsilon_t < \frac{f_{cr}}{E_c} \\ f_u + E_s \cdot \left(\varepsilon_t - \frac{f_{cr}}{E_c} - \frac{f_u - f_{cr}}{E_h}\right) & h_s < t \le h_s + h_u, \varepsilon_t < \frac{f_{cr}}{E_c} + \frac{f_u - f_{cr}}{E_h} \end{cases} \tag{2}$$

In the three-point bending test, even though no test of obtaining the materials properties was conducted specifically, the used UHPFRC was mixed with the same proportions and tested under the same conditions including the curing age, i.e. 7 days, as the UHPFRC used in the OSD introduced in the later sections, where a uniaxial compression test was conducted to obtain material properties. Thus, the material properties of UHPFRC employed in this section are consistent with those in the later sections of UHPFRC strengthened OSD. As for the steel plate, the designed values were employed for the elastic modulus and yield strength. All the material properties are listed in **Table 3** referencing **Fig. 7**.

In **Eq. (2)**, for a given ε_{cmax}, firstly the location of the neutral axis, i.e. t_m, can be obtained by solving the sectional force equilibrium equation along the beam axis direction. Correspondingly, the sectional rotation about the neutral axis or the curvature can be calculated as follows:

$$\sum F = 0 \Rightarrow \int \sigma_t(t) \cdot b \, dt = 0 \tag{3}$$

$$\varphi = \frac{\varepsilon_{cmax}}{t_m} \tag{4}$$

Then, the sectional stresses-induced sectional moment about the neutral axis can also be calculated by integrating the product of the section stress and the lever length.

$$M = \int \sigma_t(t)(t - t_m) \cdot b \, dt \tag{5}$$

Finally, one can obtain the curvature and the sectional moment for any given ε_{cmax}. This means that a relation between the curvature and sectional moment can be derived by varying the value of ε_{cmax}. As a further step, the curvature distribution along beam axis can be related to the applied load by substituting the moment distribution function into the curvature to sectional moment relation. As the second order of integration of the curvature along the beam axis is the displacement, one can obtain the load vs. displacement as well as the load vs. strain curves for any location on the beam.

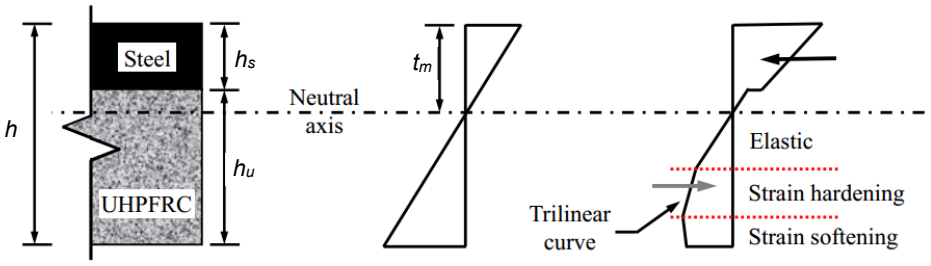

Fig. 6 Sectional analysis of flexural beam

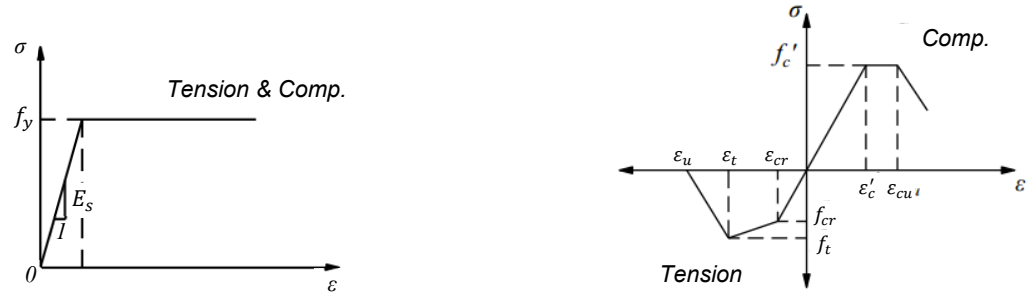

(a) Stress to strain relation of steel (b) Stress to strain relaton of UHPFRC

Fig. 7 Material constitutive models

Table 3 Material properties

Material	Parameter	Values
UHPFRC	Compression strength (f_c')	133 MPa
	Tensile cracking strength (f_{cr})	6 MPa
	Tensile strength (f_t)	9 MPa
	Elastic modulus (E_c)	31.3 GPa
	Strain at tensile strength (ε_t)	1,750 με
	Ultimate tensile strain (ε_u)	12,000 με
	Poisson's ratio	0.22
Steel	Yield strength (f_y)	295 MPa
	Elastic modulus (E_s)	200 GPa
	Poisson's ratio	0.3

2.2.3 Results comparison of composite beams under three-point bending

Fig. 8(a) shows the sectional moment to curvature relationship, where the increment of moment stops when the yielding of the steel plate occurs. As the strain on the surface of the steel plate at the quarter points were measured in experiment, the analytical load vs. strain relationship for the same points was calculated and shown in **Fig. 8(b).**

The experimental load-strain curves for the composite beams treated with the three employed bonding techniques are shown in **Fig. 9(a) – (c)** together with the corresponding analytical curve. To facilitate the comparison of the performance, **Fig. 9(d)** shows the average relations of the three specimens treated with each bonding technique. Generally, the experimental strain vs. load curves progressed and fluctuated surrounding the analytical strain vs. load curve obtained based on a perfectly bonded interface assumption. Besides, even after final failure, the slip was hardly observed in the tests of the composite beams using the three interface treatments as shown in **Fig. 10**. This excellent performance of the bonding treatments demonstrates that the perfect bond assumption can be employed at least under static load. Specifically, it is found that the curves of composite beams exhibited a linear elastic behavior initially with a slope approximate to the slope of the analytical curve for all the three interface treatments, and the width of the initial elastic range increased in an order from ENE to ENW to E. Following the initial elastic stage, the strain of the beam integrated with E bond interface experienced a sudden brittle increase, whereas the slope of strain curves of the beam integrated with ENE and ENW decreased gradually. This may be understood using both the cracking of UHPFRC and bonding interface characteristics. After the crack initiation of UHPFRC, a local stress may be generated in the UHPFRC/steel interface just at the crack location. On one hand, as the interface in the specimen E was fully and uniformly connected by the adhesive, the local strength should be relative higher than the specimens ENE and ENW where the connection was from the adhesive and the aggregates. On the other hand, if a slight slide initiates locally, it may spread with a certain distance in the E specimen depending on the relative relation between the stress at edge of the local sliding area and the bond strength, whereas the spread may be interrupted by the aggregates in the ENE and ENW specimens. As a result, the ENE and ENW specimens exhibited a relatively more ductile characteristic than the E specimens. A similar phenomenon also occurred in the pull-off test, where a sound indicating failure was shrill in E specimens but blunt in ENE and ENW specimens. Moreover, as shown in **Fig. 9(d)**, the composite beam with ENW interface exhibited a higher stiffness than the composite beam with ENE in quite a wide range from beginning, which should be the range concerned in real applications. Therefore, the UHPFRC-steel interface with the ENW bonding treatment was identified to be the most appropriate and optimal and was employed in rehabilitation the orthotropic steel decks by overlaying UHPFRCs.

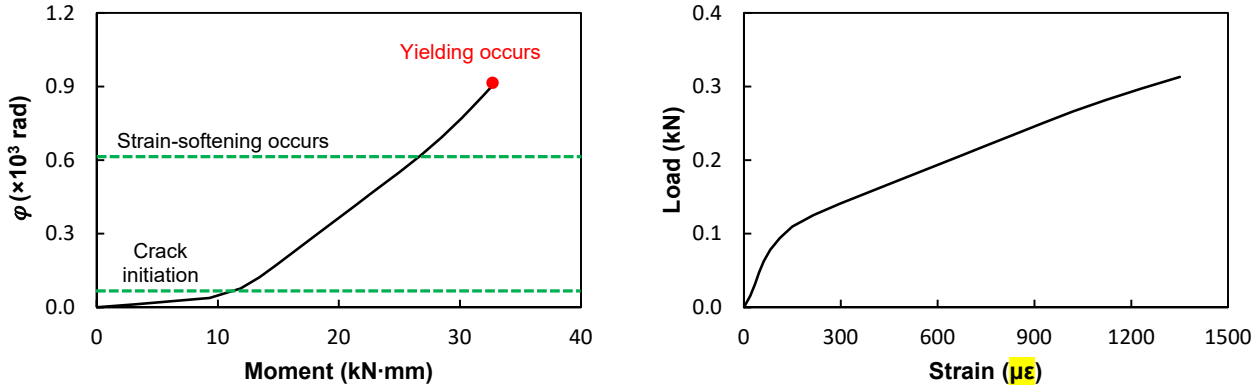

(a) Moment to curvature relation (b) Analytical load to strain relation

Fig. 8 Analytical calculation of load to strain relation

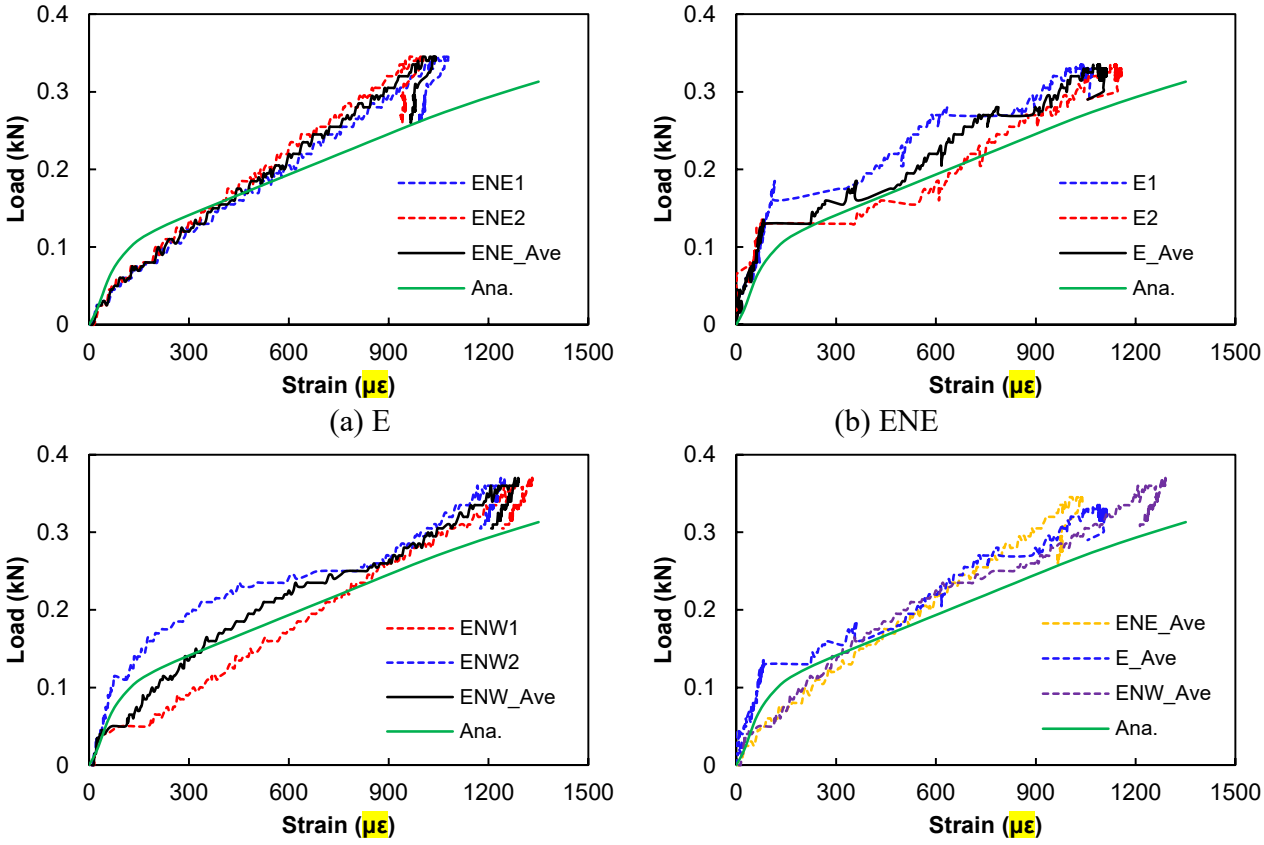

(a) E (b) ENE

(c) ENW (d) Average

Fig. 9 Experimental strain vs load relations

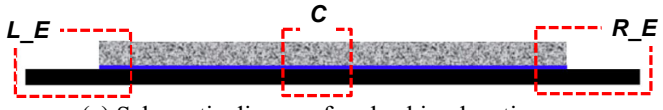

(a) Schematic diagram for checking locations

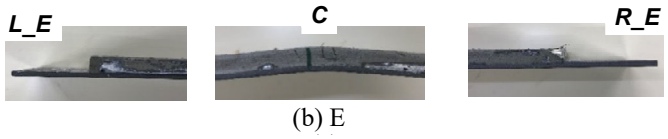

(b) E

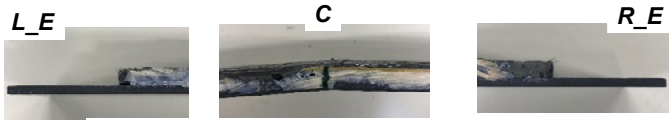

(c) ENE

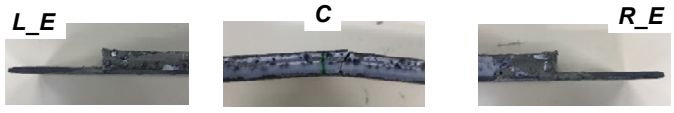

(d) ENW

Fig. 10 Interface condition after failure

3 FINITE ELEMENT ANALYSIS TO EVALUATE STRESS REDUCTION EFFECTS

3.1 Experimental program

This study belongs to a systematic experimental program of assessing the strengthening effects of UHPFRC overlay on the performance of OSDs. In this program, the OSD was firstly subjected to static loads up to the service state to obtain reference values of the performance indicators. Secondly, UHPFRC was overlaid on the OSDs forming a composite deck which was then tested under static load up to service static, cyclic loads at service state under both dry and wet conditions, and cyclic heavy load in a sequence to obtain a comprehensive evaluation of the effects of UHPFRC overlay corresponding to the real conditions. Finally, the composite deck with UHPFRC removed was subjected to a cyclic heavy load until failure. A wheel-type load was employed in the entire experimental program. Considering the length of the article, this study focuses on investigating the static test parts of both OSD with and without UHPFRC overlay, and the other parts will be reported later.

Fig. 11 shows the set-up of the experiment and **Fig.12** shows the geometric details of different views and various cross sections of the tested OSDs. It is found that the OSDs consists of a steel deck with spans of 3300 mm and 2720 mm along the longitudinal direction and transverse direction, respectively, and a 12 mm thickness. Along the longitudinal direction, the steel deck is supported by a couple of main girders around both ends and 7 ribs in an open bulb type. Specifically, the main girders have a depth of 690 mm and a thickness of 14 mm, and the bulb ribs are with a consistent dimension of 230×11×30 mm. Along the transverse direction, the steel deck is supported by 3 cross beams with a 1500 mm spacing. The depth and thickness of the cross beams are 600 mm and 9 mm, respectively.

In terms of the composite deck, to facilitate the reference of the practical engineering applications, a thickness, i.e. 25 mm, which was normally employed in real bridge deck repairing in Japan was employed for the UHPFRC overlay in this study. This thickness was set also to be consistent with the pull-tests considering that the fiber orientation and distribution which depend greatly on the flow of the matrix and the subsidence of the fibers may be significantly affected by the dimensions of the overlayer. Considering that the UHPFRC was normally used in repairing bridge where the duration of traffic interruption should be minimized, the tests were initiated at an early age, i.e. 7 days, instead of at 28 days. Correspondingly, uniaxial compression test was conducted on UHPFRC cylinders at 7 days to obtain the compression strength and Young's modulus, which were 133 MPa and 31.3 GPa, respectively. As the ENW type of interface treatment provided the excellent performance in the bonding interface tests in section 2, the same technique was used to integrate the UHPFRC overlay and the OSD herein as well. As illustrated in **Fig. 13**, the premixed UHPFRC was casted on the OSD where the top surface was treated with adhesive and aggregates, and then covered with sheet and cured under room temperature until the test initiation. To minimize shrinkage, water was sprayed regularly to maintain a moist condition.

Fig. 11 Experimental set-up

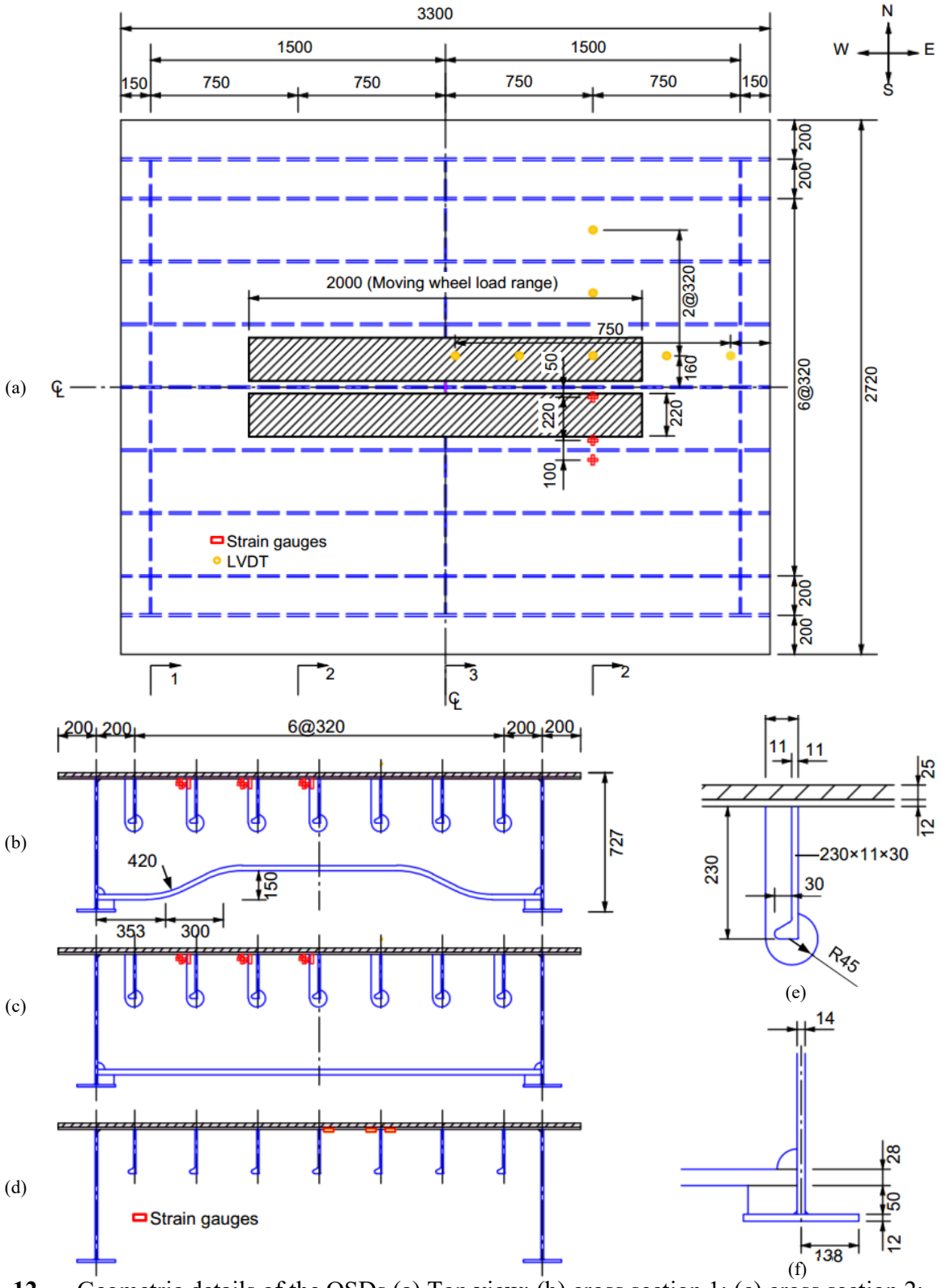

Fig. 12 Geometric details of the OSDs (a) Top view; (b) cross section 1; (c) cross section 2; (d) cross section 3; (e) region A; (f) region (Unit: mm)

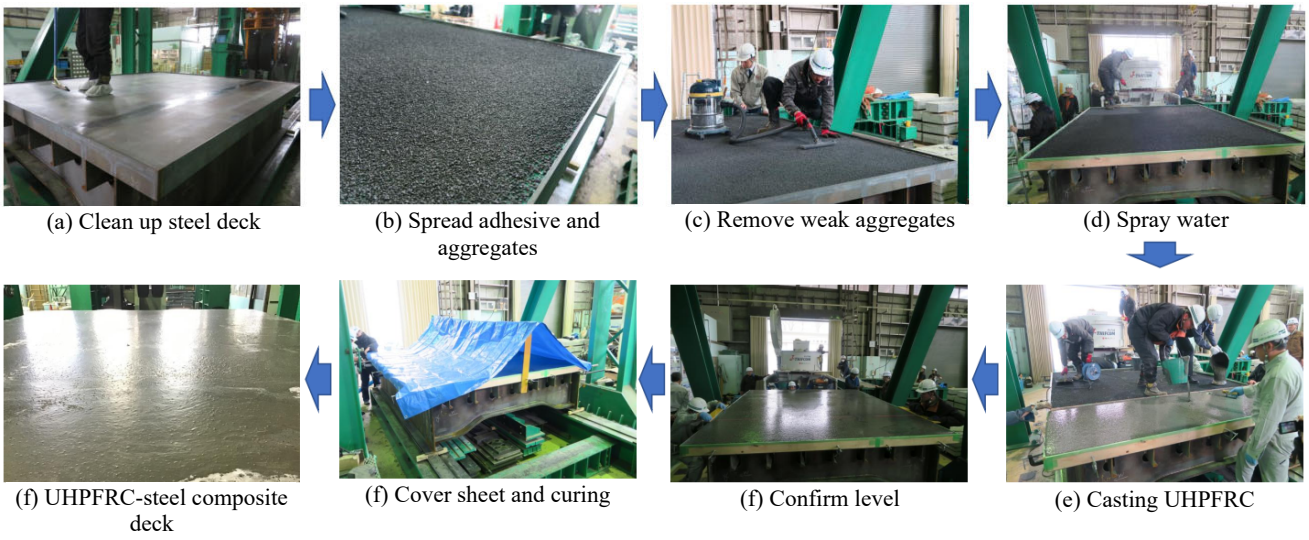

Fig. 13 Specimen preparation procedure

3.2 Numerical analysis

Focusing on the OSDs subjected to the static wheel-type load, numerical analyses were conducted employing the finite element method (FEM) instead of the theoretical method in section 2 as the OSDs possess a complex geometry. **Fig. 14** shows the finite element model of the OSD overlaid with UHPFRC built in a software named MSC/Marc. A FE model with a 20 mm of characteristic dimension was built for the whole structure because the structure has no symmetric characteristics. In terms of the hotspot areas, the mesh is refined locally as shown in **Fig. 15**, where a sufficiently wide mesh transition area is exploited to avoid local stress anomalies. To facilitate interpretation, models of the OSDs with and without UHPFRC overlay are named as model SU and S, representatively.

As for the material models, an elastoplastic model shown in **Fig. 7(a)** and a multi-linear constitutive model shown in **Fig. 7(b)** was employed for all the steel members and the UHPFRC hereby to simulated the strain-hardening and strain-softening characteristics, respectively. Correspondingly, the values listed in **Table 3** were used for the controlling points of the material constitutive model. As the ENW interface treatment technique exhibited an excellent bonding strength in the pull-off tests and a negligible slip in the three-point bending test, a perfect connection was assumed for UHPFRC/steel deck interface in the FEA of the composite deck. To simulate the constitutive relation and the cracking behaviors of UHPFRC, a material user subroutine was developed based on a smeared crack model using FORTRAN. This material subroutine was initially developed for the simulation of the cracking behaviors of element scale ECC beams in [38, 39] and then improved and verified in application of analyses on structures including beam, panel slab, and OSDs that possess various dimensions and consist of different cementitious composites including ECCs, RC, and UHPFRCs in [8, 11, 40-42]. In this model, the total strain of the cracked material is decomposed into non-cracked and cracked components to develop the overall stress-strain relationship after cracking. Crack formation and propagation characteristics are considered based on a multiple fixed crack concept, where the cracks are assumed to initiate in a direction perpendicular to the maximum principal strain once the tensile stress exceeds the cracking strength. Similarly, at the same integral point, the second crack and third sets of cracks may initiate in a sequence perpendicularly to the formed cracks when the correspondingly tensile stress component reaches the cracking strength. Nevertheless, as the UHPFRC possesses a high cracking strength and the no dramatic variation of the stress status occurs when

the wheel moves back and forth on the targeted OSDs, the second and third sets of cracks may not be generated. Besides, to investigate the crack propagation along the depth direction, the UHPFRC overlay which was modelled with 3D solid element was divided into 3 layers in the vertical direction.

In terms of the loading condition, a couple of distributed loads with a dimension 220 (L)×250 (T) was applied on the OSDs decks symmetrically about the longitudinal centerline to simulate the wheel loads in the experiment. As shown in **Fig. 12**, the bridge deck was supported by three crossbeams along the transverse direction. As a result, the middle crossbeam and the members close to the hotpots may have reached the critical status when the when load was located above the middle crossbeam because the location was just at the midspan of the OSD and the load was transferred directed to the middle crossbeam and the hotspot areas. In terms of the steel deck, it may have reached the critical status when the wheel was located in the middle of the span between two adjacent crossbeams because the bending span reaches the maximum value as shown in **Fig. 12**. Hence, this study investigated these three load conditions as indicated with the white rectangles in **Fig. 14**. According to the loading location away from the middle cross beam, the three conditions are named as Center Load case, East Load case, and West Load case, respectively. Besides, a 70 kN of total load of a couple of the distributed loads was applied in each case to be consistent with the experiments.

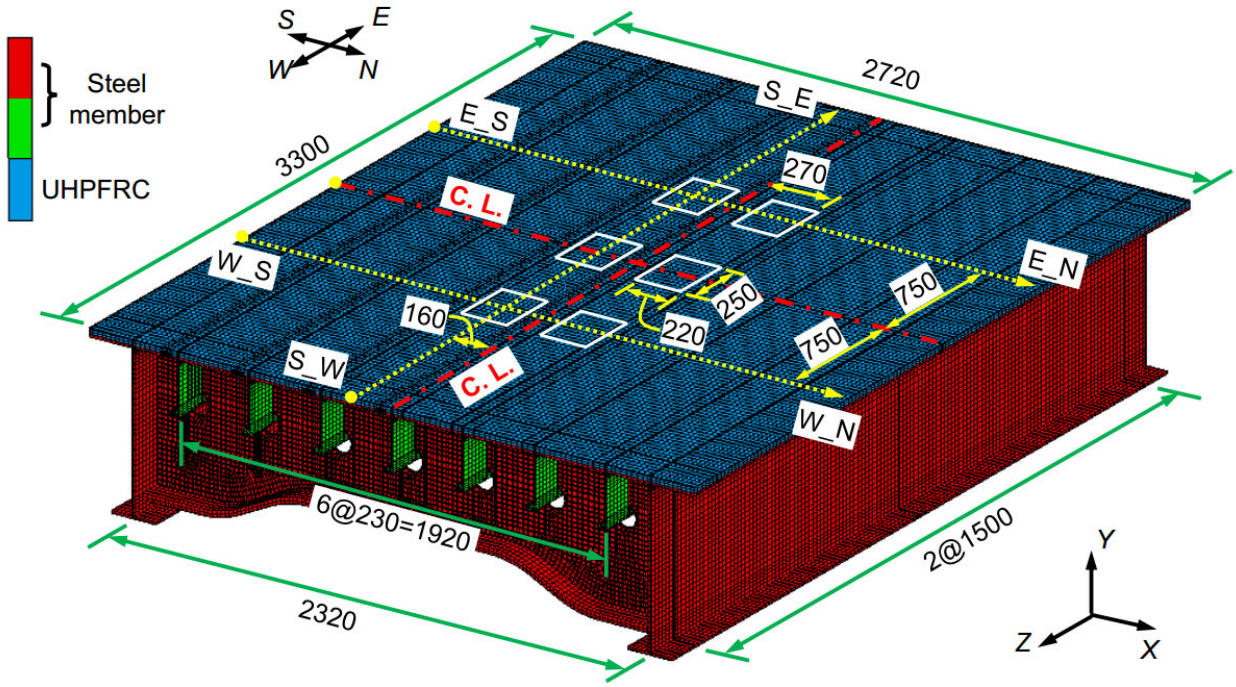

Fig. 14 Finite element model of the steel bridge deck with overlaid UHPFRC (Unit: mm)

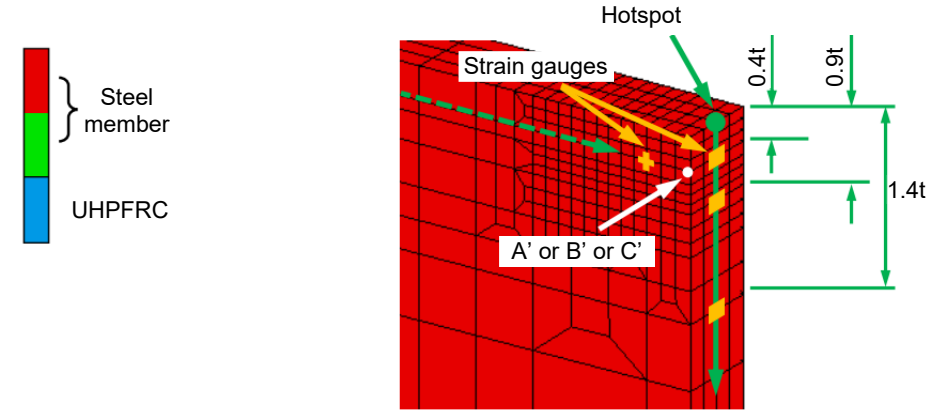

(a) Downward path from the hotspot

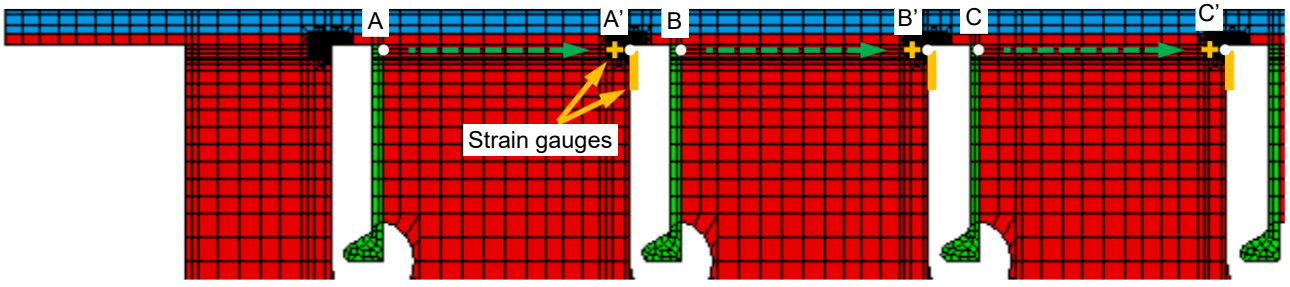

(b) Paths for strain on the middle transverse stiffer

Fig. 15 Local FE mesh at hotspot areas and location of strain gauges (t: thickness of steel deck)

3.3 Results of nonlinear FEA results

3.3.1 Displacement of steel deck

In the experiments, the steel deck displacements were measured on the bottom surface at some locations along the longitudinal path S_W – S_E and the transverse path E_S – E_N. According to **Fig. 14**, the two ends of each path are named as Orientation of the path relative to the parallel centerline_Position of the end on the path. Taking the S_W endpoint of the path S_W – S_E for example, S indicates that the path is at the Southside of the longitudinal centerline and W indicates that this point is the West end of the path. Similar to the experimental measurements, deflection distributions along path S_W – S_E and E_S – E_N were obtained from FEA and compared with the corresponding experimental results in **Fig. 16** and **Fig. 17** respectively. Considering that the structure is symmetric to the transverse centerline, only results of Center Load and East Load cases are presented. It is found that the experimental displacements were larger than the analytical results, which may stem from simplifications in the numerical analysis as schematically shown in **Fig. 18**. As illustrated in this figure, the measurements include not only the deck deflections but also the deformations of concrete foundation, steel base, etc. Besides, some additional deformations in the experimental set-up like structural gaps may inevitably exist in real structures, especially complex structures like the OSDs. From **Fig. 16(a)**, it is also found that contrary to the general recognitions the experimental displacement of OSD with UHPFRC was larger than that of the OSD without UHPFRC in a region close to the center crossbeam. This may be caused by the additional deformation describe above and the variation of the contribution ratios of the overall and local deformations in the total deformations. Attributing to the UHPFRC overlay, the stiffness of the OSD was increased resulting in a move evenly distributed load and a less local deformation adjacent to the

crossbeam as verified by the displacement curves. Nevertheless, it is found from **Fig. 16(a)** that the local displacement may be in an opposite direction as the overall displacement, which is more apparent in **Fig. 17(b)**. In addition, the local deformation is sensitive to the local conditions including the welding area and the tire load contacting area which was irregular as typically shown in **Fig. 19** and may be different from UHPFRC and steel surfaces. Furthermore, the difference between the structure deformation of S and SU may become less apparent due to the additional deformation. Therefore, it may be stated that the simulation can match experimental displacements reasonably well, especially the trends which indirectly reflect the deformations. However, the absolute values of the displacements may only be able to exploited as a reference. The deformation behaviors should be more comprehensively investigated by means of strains as the performance of the OSDs is determined by the deformations especially the local strains.

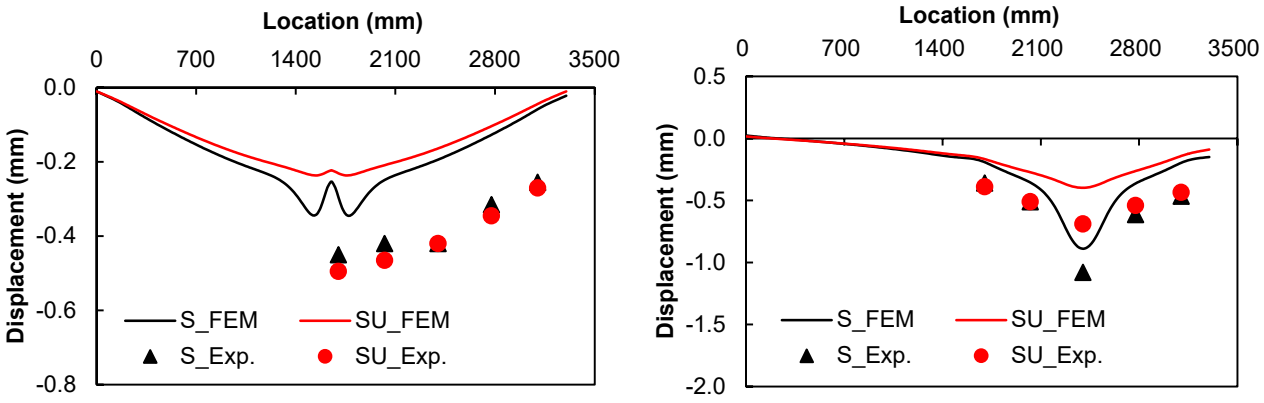

(a) Center load case (b) East load case

Fig. 16 Vertical displacement of steel deck in OSDs without (S) and with (SU) UHPFRC overlay along path S_W to S_E

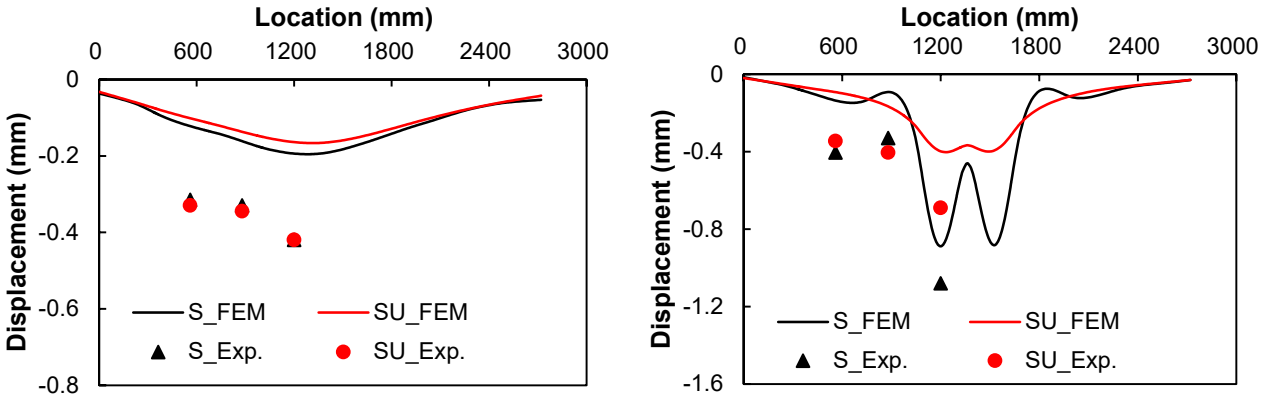

(a) Center load case (b) East load case

Fig. 17 Vertical displacement of steel deck in OSDs without (S) and with (SU) UHPFRC overlay along path E_S to E_N

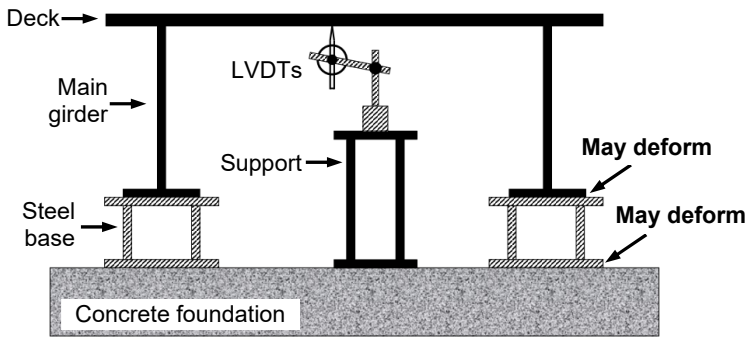

Fig. 18 Schematic diagram illustrating real deformation and measured displacements

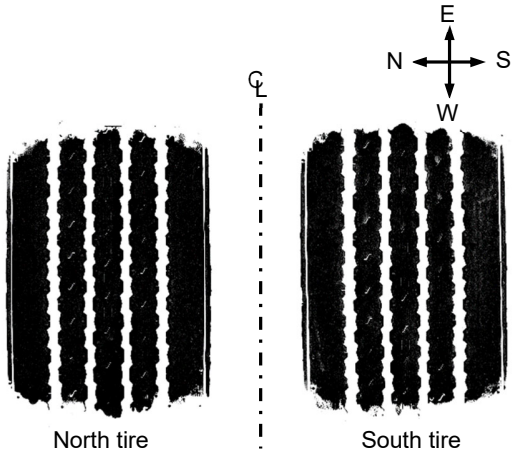

Fig. 19 Typical contacting area

3.3.2 Strain of steel deck

In this study, all the values of the given strains are the strain changes measured before and after applying the wheel load. Due to the existence of the middle transverse crossbeam as shown in **Fig. 12**, the bending span reaches the maximum value under either the East Load case or West Load case as the bending span reaches the maximum value. Correspondingly, the critical values of the strains of the steel deck may appear under these two load cases and in areas beneath the applied load. Thus, strain gauges along both transverse and longitudinal directions were attached on the bottom surface of the steel deck at several locations along the E_S – E_N path. A comparison of the experimental and analytical strains of steel deck on the bottom surface along the E_S – E_N path under the East Load case is shown in **Fig. 20**, where a good agreement can be observed between analyses and experiments. In addition, it is found that about 80% of stress reduction can be achieved by overlaying a 25 mm UHPFRC layer. Specifically, the maximum tensile and compression strains in the global X direction decreased from 400 με to 97 με and from -488 με to -78 με, respectively. As for the global Y direction, the maximum tensile and compression strains decreased from 102 με to 14 με and from -52 με to -30 με, respectively.

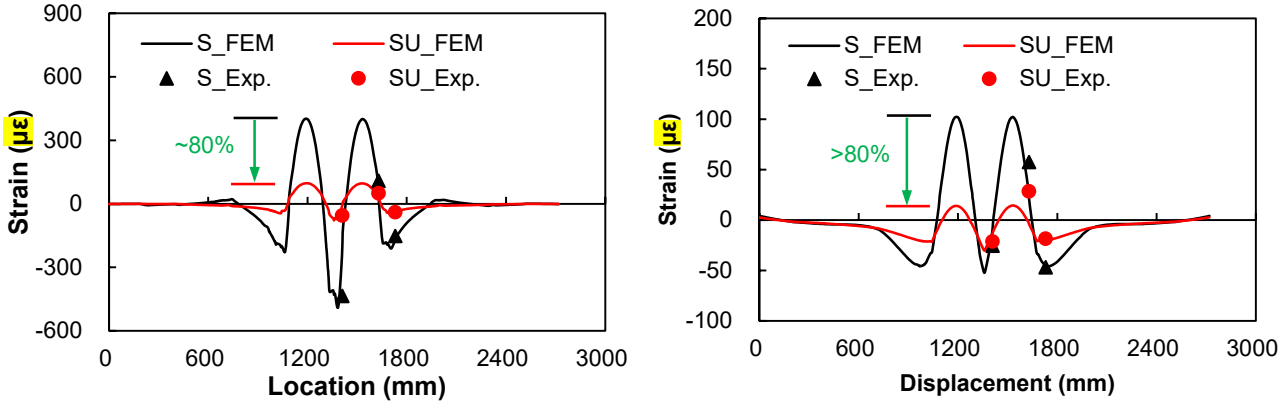

(a) Strain in global X axis (b) Strain in global Y axis

Fig. 20 Strain of steel deck in OSDs without (S) and with (SU) UHPFRC overlay on the bottom surface along path E_S to E_N for East Load case

3.3.3 Strain of middle transverse crossbeam

As the hotspot areas (see. **Fig. 15**) are normally the critical locations of the middle transverse crossbeam, this study investigated the strain distributions along the paths approaching the horizontally and emitting vertically from hotspots.

As for the paths approaching the hotspots, i.e. path A-A', B-B', and C'-C (see. **Fig. 15**), **Fig. 21** and **Fig. 22** show the analytical strain distributions under the Center Load and East Load cases, respectively, together with the corresponding experimental measurements. Similar to the observations in the strains of steel deck, the analytical results matched well with the experimental results. However, instead of reducing the overall strains of the crossbeam, the stress reduction effects of the UHPFRC overlaid were more profound in areas close to the hotspots. Attributing to the stiffness provided by the UHPFRC overlay, the strain became more smoothly and evenly distributed and the strain peaks which were observed in the non-reinforced OSDs at the hotspot areas were remarkably reduced. However, it is found that experimental strain values at the gauge locations (see. **Fig. 15**) of the OSD-UHPFRC composite deck was larger than the strain values of the OSD. These observations can be understood following the idea that the total deformation consists of both local and overall components. Obviously, the local deformation should be a rotation around the hotspots and overall deformation may be a translational movement which may be able to be decomposed along the global axes. On one hand, the rotation may induce both local compression and tensile strains depending on the position away from the hotspot. The values of these rotation-induced strains should be sensitive to the distance away from the hotspot and more significant in model S than in model SU. On the other hand, the translational movement may cause either compressive or tensile strain in the crossbeam along a given global axis. In addition, as exhibited in **Figs. 21** and **22**, the strain components caused by the local rotation which may transfer from high level of compression to tension in a quite limited region should play a dominant role especially in the hotspot areas. Moreover, even though it cannot be clear observed from the figures, the length of the transferring region in S should be shorter than in SU from a theoretical view, which means that the degree of localization should be different in S and SU. In other words, for a given position, the contribution of the rotation-induced strain should not be proportional to the stiffness of the deck and cannot be simply calculated by multiplying a coefficient related only to the stiffness of the deck. As a result, for the position with strain gauges, if the measured strain contained more compressive components in a given direction due to the local rotation in S than in SU, the experimental strains may exhibit a relative relation as observed in **Figs. 21(a)** and **22(a)** in the global X axis. Nevertheless, if the measured strain contained more tensile components in a given direction

due to the local rotation in S than in SU, the experimental strains may exhibit a relative relation as observed in **Figs. 21(b)** and **22(b)** in the global Y axis.

In terms of the paths emitting downward from the hotspots, **Fig. 23** and **Fig. 24** show the analytical strain distributions under the Center Load case and the East Load case, respectively, together with the corresponding experimental measurements. It is found that the UHPFRC-induced change occurred mainly on the load transferring or distribution rather than on the overall values. In other words, the angle of the trend of the strain distribution curve from the global Y axis (see. **Fig. 14**) was reduced due to the UHPFRC overlay, whereas the average value of the strain in the employed length seems to have stayed almost unchanged except for the strain distribution in **Fig. 23 (c)**. These observations can also be understood using the local and overall deformation characteristics as well. Taking the hotspot B' for example, as shown in **Fig. 15**, the local deformation is mainly a rotation around the point B' and the primary component of the global deformation is a downward translational displacement under the Center Load case. If the effects of these two kinds of deformations on the global Y axis strains of the cross beam are considered separately, the rotation may induce a high level of local compressive strain in an area adjacent point B' and a tensile strain in areas relative far away from the point B', whereas the downward translational displacement may create an almost evenly distributed compressive strain. Obviously, both deformations are related to the stiffness of the deck, but the local deformation should be much more sensitive than the global deformation, which can be indirectly verify by the displacement distribution shown in **Figs. 16** and **17**. In addition, the stiffness of the deck which determines the local rotation was improved after overlaying UHPFRC, whereas stiffness of the transverse crossbeam which determines the downward translation displacement stayed unchanged. As a result, as exhibited in **Fig. 23(b)**, the effects of the UHPFRC were more remarkable in area close to the hotspot, which is a superior phenomenon for steel structures. More specifically, one can observed more compressive strain in the area close to the point B' and less compressive strain in the area away from the point B' in specimen S than SU as shown in **Fig. 23(b)**. Similarly, the trends exhibited in **Fig. 23(a)** can be also understood. In terms of the curves in **Fig. 23(c)**, as the point C' is close to the longitudinal centerline and a couple of distributed loads are applied symmetrically to the centerline, the local deformation may be shifted from rotation dominant to movement dominant. Correspondingly, the strain distribution curves in **Fig. 23(c)** are almost parallel to the vertical direction. However, as the structural is not perfectly symmetric about the centerline and the stiffness of the decks is not infinite, a compressive strain with a relatively high level can still be observed locally close to the hotspot area. In summary, it is stated that the overlaid UHPFRC may provide additional stiffness which can enlarge the load transferring area, make the strain more evenly distributed, and also effectively reduce the peak values of the strain at the critical locations. As the fatigue life of the steel members is directly determined by the stress amplitude at the critical locations, these UHPFRC-related local changes demonstrate the efficiency and life extension effect of the reinforcing technique.

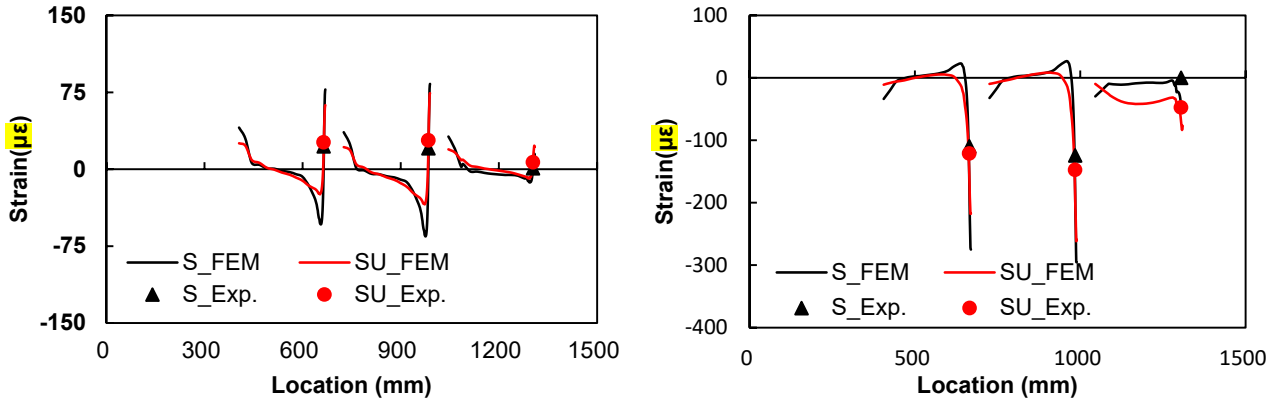

(a) Strain in global X axis (b) Strain in global Y axis

Fig. 21 Strain of the middle transverse stiffer in OSDs without (S) and with (SU) UHPFRC overlay along path A-A', B-B', C-C' for Center Load case

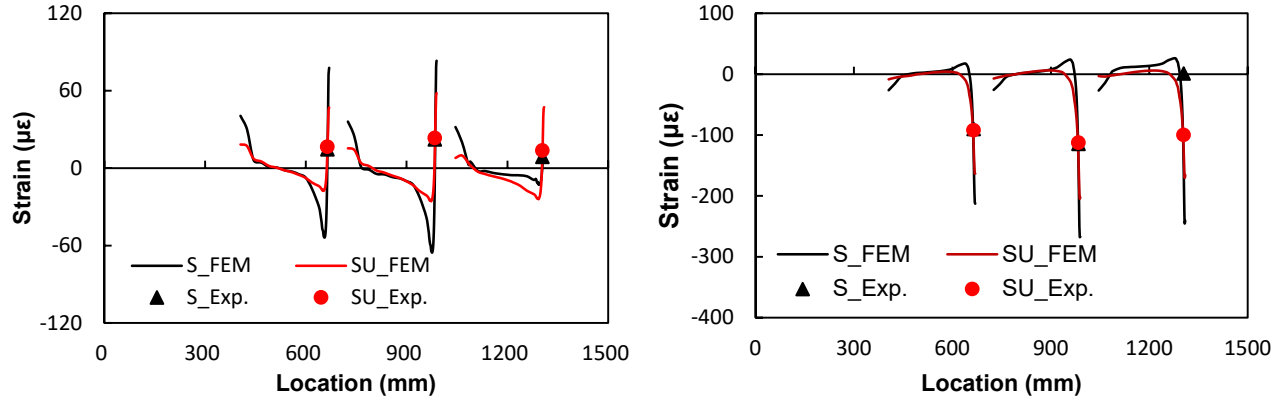

(a) Strain in global X axis (b) Strain in global Y axis

Fig. 22 Strain of the middle transverse crossbeam in OSDs without (S) and with (SU) UHPFRC overlay along path A-A', B-B', C-C' for East Load case

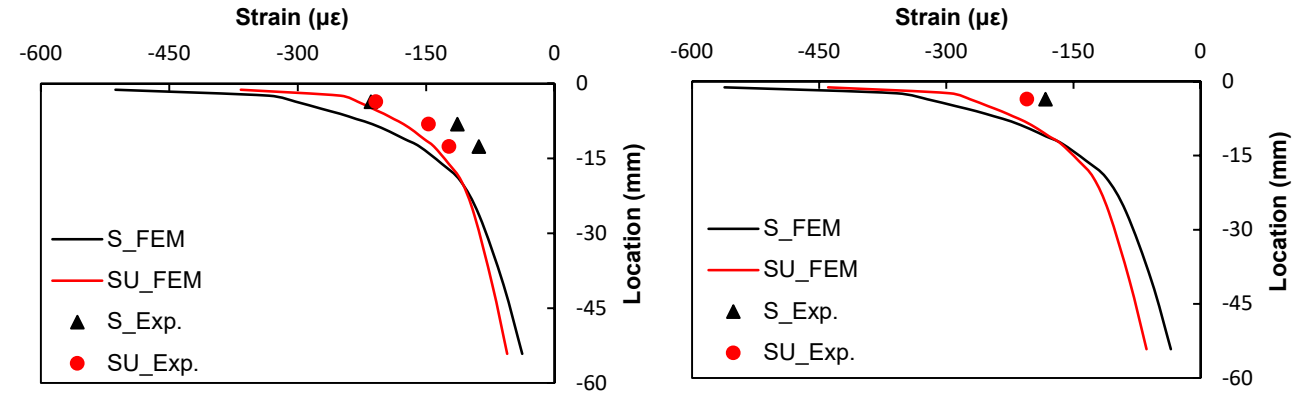

(a) Strain in global Z axis near A' (b) Strain in global Z axis near B'

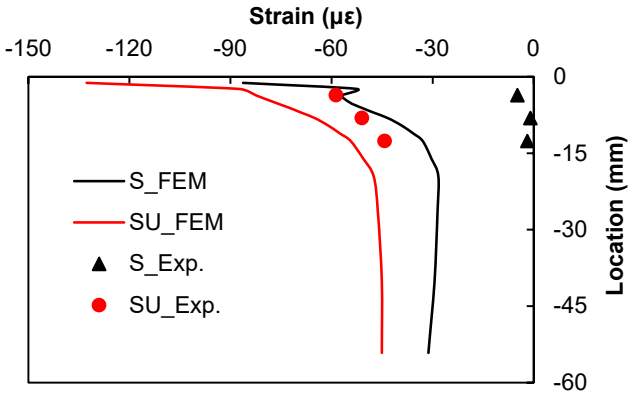

(c) Strain in global Z axis near C'

Fig. 23 Strain the transverse crossbeam in OSDs without (S) and with (SU) UHPFRC overlay downward path from the hotspot for Center Load case

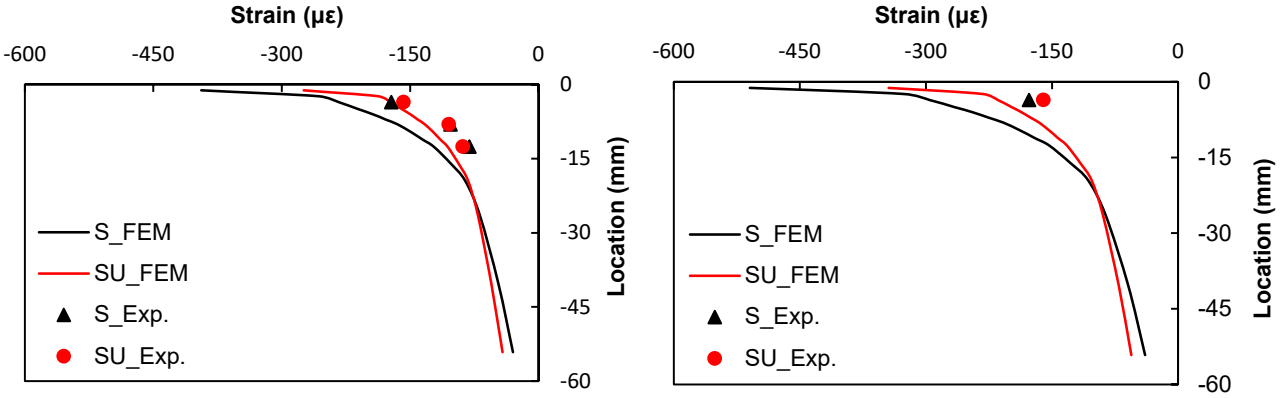

(a) Strain in global Z axis near A' (b) Strain in global Z axis near B'

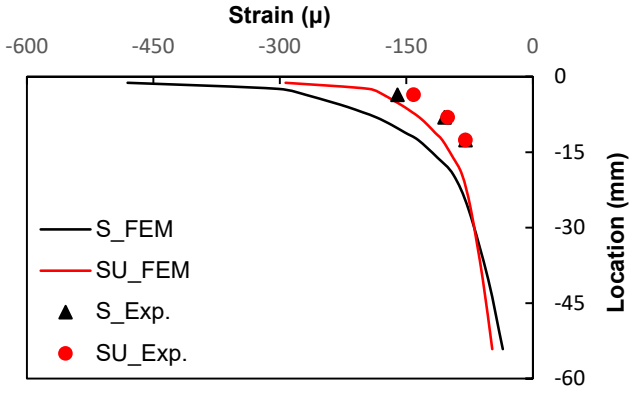

(c) Strain in global Z axis near C'

Fig. 24 Strain the transverse crossbeam in OSDs without (S) and with (SU) UHPFRC overlay along the downward path from the hotspot for East Load case

3.3.4 Cracking of UHPFRC

Fig. 25 shows the top view of the maximum principal strain distribution of the UHPFRC overlay under the Center Load case. Even though a very localized strain was observed close to the center of the UHPFRC layer and symmetric to the middle transverse crossbeam, no crack was formed as the maximum strain was smaller than the cracking strain of UHPFRC, i.e. 0.00019.

For the East Load case, top views of the maximum principal strain distributions on different thicknesses of surfaces of the UHPFRC are shown in **Fig. 26**, where the regions colored with grey are the cracked areas. Due to the existence of the longitudinal stiffeners, the load produced a negative bending moment in the UHPFRCs above the stiffeners, which induced the crack initiation. It is found that even though the 25 mm thickness of the UHPFRC overlay is very thin compared to the conventional techniques with other cementitious like concrete and steel fiber reinforced concrete (SFRC), the crack propagated rather slowly in the depth direction, which may be attributed to the strain-hardening behavior after cracking of UHPFRC. Instead of releasing stress and redistribute the load quickly to the adjacent materials, the cracked UHPFRC can still sustain the stress. Besides, compared with other cementitious composites, e.g. engineering cementitious composites (ECCs), which also exhibit the strain-hardening domain, the cracking and ultimate tensile strengths of UHPFRC are much higher. As the stiffness of cementitious materials decreases dramatically after cracking, a thin layer of UHPFRC may enhance the stiffness of the OSDs effectively as the high strengths can postpone the crack initiation and the strain-hardening can decelerate crack propagation. In addition, considering that the steel fibers are used in UHPFRC rather than polyethylene or polyvinyl alcohol fibers, the fatigue performance of UHPFRC tends to be more superior, especially under reversed repetitive loads [43].

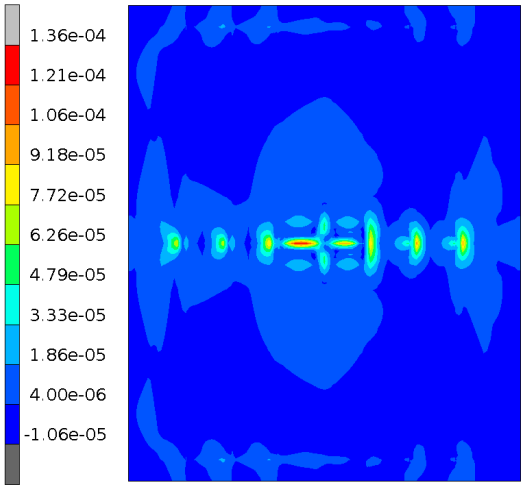

Fig. 25 Maximum principal strain distribution under Center load case

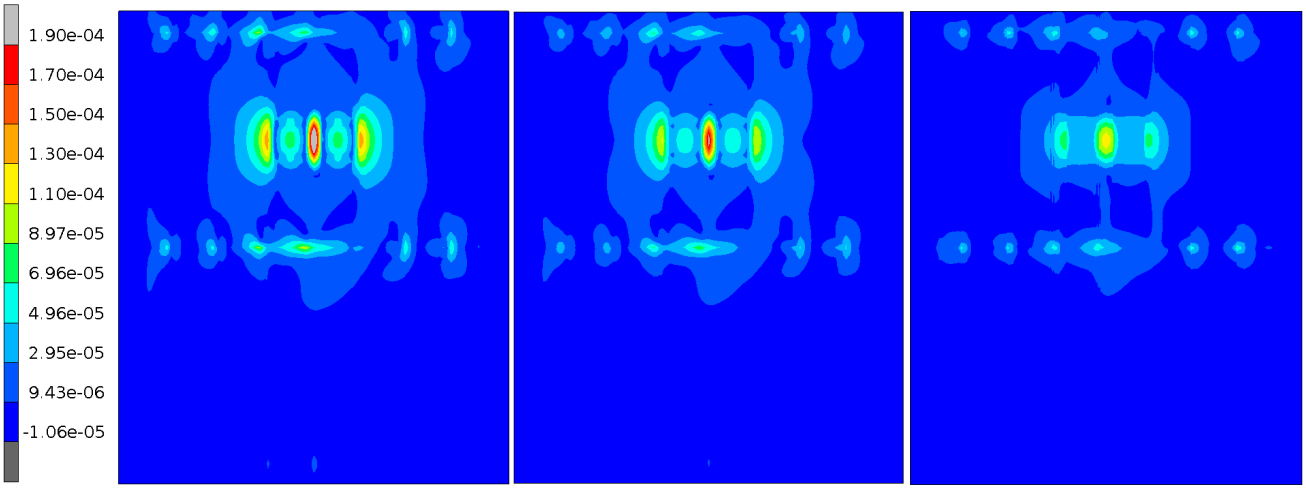

(a) Top surface (b) at a 5mm of thickness (c) at a 15mm of thickness

Fig. 26 Maximum principal strain distribution on different thicknesses of surfaces under East load case

3.4 Fatigue life prediction

According to the investigation of the FEA and experiment results, several locations, such as the area along E_S – E_N just beneath the location areas and the hotpots of the middle transverse crossbeam, were identified as the critical locations which determine the fatigue life of the OSDs. Therefore, the analytical strains of these locations were exploited to predict the fatigue life of the OSDs in this section.

In terms of the strain of the steel deck, it can be obtained directly from finite element analysis. The maximum values of strain were -488 με and -78 με for the model S and SU, respectively, as shown in **Fig. 20**. However, as the strain value at the exact hotspot was difficult to be obtained from finite element analysis, it was recommended by the International Institute of Welding that the strain at the hotspot may be calculated by a three-point linear extrapolation method [44]. As shown in **Fig. 15**, the three points which have distances of 0.4, 0.9, and 1.4 times of the thickness of the transverse crossbeam were exploited for the linear extrapolations. **Figs. 27** and **28** show the linear extrapolations calculating the strains at the hotspot near point A', B', and C' under the Center Load case and the East Load case, respectively. For the S and SU under the Center Load and East Load cases, **Table 4** lists the strains calculated from the linear extrapolation method for the hotspots near point A', B', and C'. It is found that the maximum value appeared at the hotspot near point C' under the Center Load case. Thus, this hotspot was the most dangerous and susceptible to fatigue.

With these critical strains, the fatigue life of the OSDs without and with UHPFRC overlay were predicted respectively employing Eqs. (7) and (8) to evaluate the stress reduction and the service life extension effects attributing to the UHPFRC overlay.

$$\sigma_k^m \cdot N = C \tag{6}$$

$$C = (FAT)^m \cdot (2 \times 10^6) \tag{7}$$

where σ_k^m is the equivalent stress range that is equal to an absolute value of the maximum strain multiplying the elastic modulus of steel. N is the total number of cycles until fatigue. FAT is the basic fatigue strength of 2 million cycles. As suggested by the Steel Structure Committee of JSCE [45], 3 and 80 MPa were employed for m and FAT, respectively, in this study. The number of cycles was then transferred to the years of service life by dividing 32000. **Table 5** lists the predicted fatigue life of the OSDs decks with and without UHPFRC overlay based on the fatigue life of the steel deck and the middle

transverse crossbeam. It is found that attributing to the 25mm of UHPFRC overlay the fatigue life of the main members may be significantly prolonged. More specifically, the fatigue life of the steel deck and the transverse crossbeam may be prolonged from 34.5 years to 8429 year and from 71.23 years to 130.63 years, respectively. As a result, the structure members are expected to survive after the designed service life owing to the UPHFRC overlay.

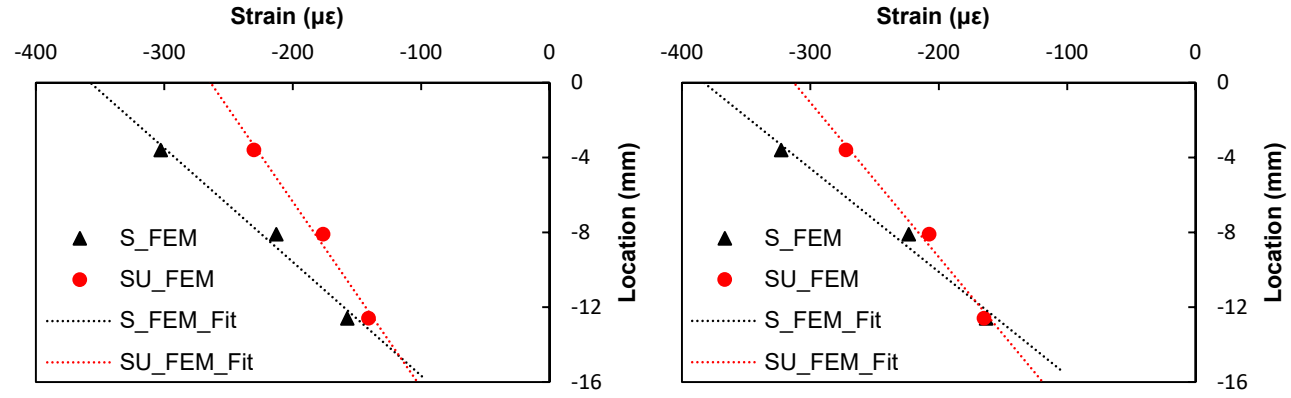

(a) Strain in global Z axis near A’ (b) Strain in global Z axis near B’

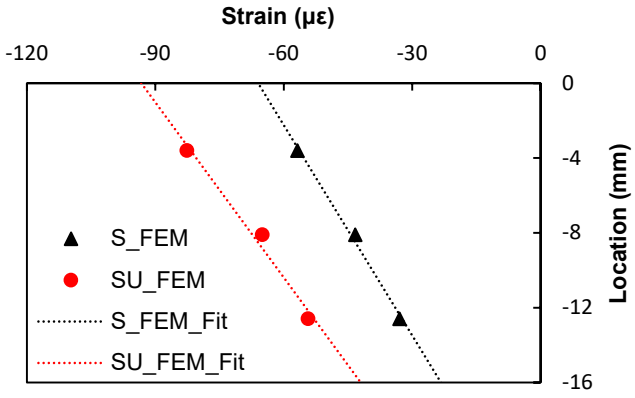

(c) Strain in global Z axis near C’

Fig. 27 Linear extrapolation to obtain strain at hotspot in OSDs without (S) and with (SU) UHPFRC overlay for Center Load case

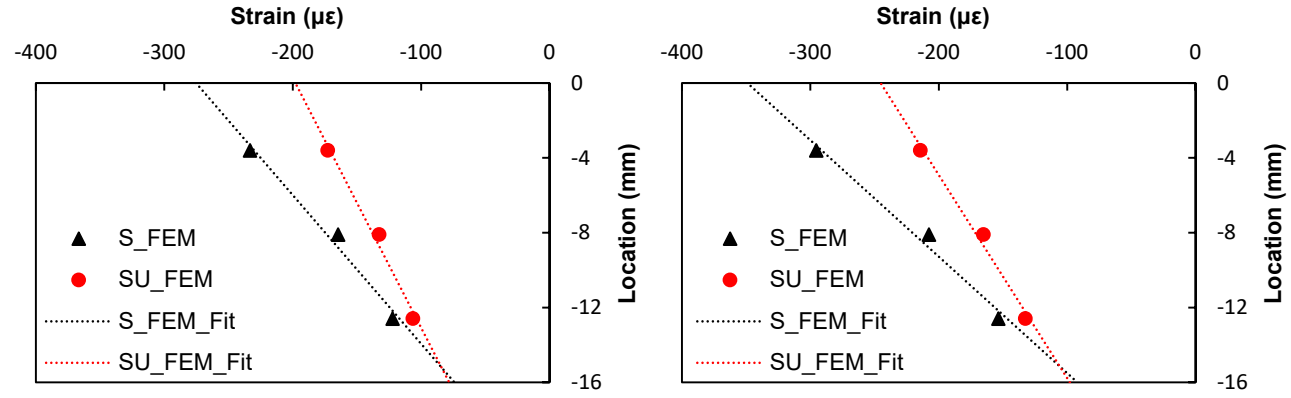

(a) Strain in global Z axis near A’ (b) Strain in global Z axis near B’

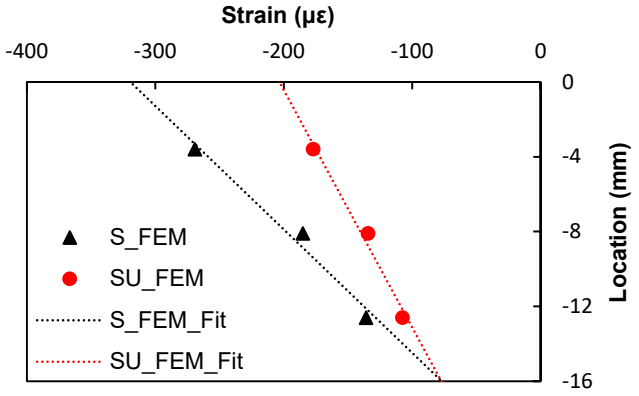

(c) Strain in global Z axis near C'

Fig. 28 Linear extrapolation to obtain strain at hotspot in OSDs without (S) and with (SU) UHPFRC overlay for East Load case

Table 4 Strain at hotspots determined from linear extrapolation

	Center Load case			East Load case		
	Near A'	Near B'	Near C'	Near A'	Near B'	Near C'
Strain of model S (με)	-357.63	-382.93	-65.96	-275.06	-348.93	-319.44
Strain of model SU (με)	-263.87	-312.87	-93.24	-197.79	-245.24	-203.33
(S-SU)/S (%)	26.22	18.30	-41.35	28.09	29.72	36.35

Table 5 Fatigue life predictions

		Strain (με)	Equivalent stress range, σ_k (MPa)	Fatigue life (year)	Safety
Steel deck	S	-488	97.6	34.4<100	NG
	SU	-78	15.6	8429>100	OK
Transverse crossbeam	S	-382.93	76.59	71.23<100	NG
	SU	-312.87	62.57	130.63>100	OK

4 CONCLUSION

Aiming at providing an effective repairing scheme for the orthotropic steel decks (OSDs), this study investigated a stress-reduction effect of overlaying a 25 mm of UHPFRC layer on the OSDs, where a new adhesive-based bonding technique for the UHPFRC-steel interface was developed and then applied to ensure the composite behaviors. Based on the analytical and experimental results obtained in this research the following conclusions are drawn:

(1) The bond adhesive of E250 was identified as a suitable bond for the UHPFRC to steel interface as an about 3 MPa of excellent tensile bond strength was achieved under the pull-off tests and an almost intact without slip UHPFRC/steel interface was exhibited after the three-point bending tests on UHPFRC-steel composite beams. Besides, by adding aggregates on the surface of the bond E250 and spraying water before casting UHPFRC, the failure of the UHFPRC/steel interface became less brittle.

(2) In terms of the OSDs with and without UHPFRC overlay, the nonlinear finite element method including the pre- and post-cracking behaviors of UHPFRC, i.e. elastic, strain-hardening, and softening, exhibited a good agreement with the experiment results. From the analyses, it was found that owing to the overlaid UHFPRC the strain of the steel deck was reduced by about 80% at the critical locations and the strain of the transverse crossbeam became more evenly and smoothly distributed in the hotspot areas.

(3) Due to the stress reduction effects of the overlaid UHPFRC, the fatigue life of the OSD was remarkably extended to over 100 years based on a fatigue life prediction using the analytical strains at the critical locations.
(4) As the UHPFRC possesses both higher strengths than other conventional cementitious composites and a strain-hardening characteristic after cracking, the UHPFRC overlay released stiffness later and slower. Consequently, it is appropriate to overlay a thinner layer of UHPFRC than the normally used thickness of overlaying cementitious composites to provide sufficient stiffness enhancement as well as reduce additional self-weight.

CONFLICT OF INTEREST

The authors declare no conflict of interest.

FUNDING

This research did not receive any specific grant from funding agencies in the public, commercial, or not-for-profit sectors.

REFERENCES

[1] Cheng, B., Ye, X., Cao, X., Mbako, D. D., & Cao, Y. (2017). Experimental study on fatigue failure of rib-to-deck welded connections in orthotropic steel bridge decks. International Journal of Fatigue, 103, 157-167.

[2] Yokozeki, K., & Miki, C. (2017). Fatigue assessment of various types of longitudinal-to-transverse rib connection in orthotropic steel decks. Welding in the World, 61(3), 539-550.

[3] Kainuma, S., Jeong, Y.-S., Ahn, J.-H., Yamagami, T., & Tsukamoto, S. (2015). Behavior and stress of orthotropic deck with bulb rib by surface corrosion. Journal of Constructional Steel Research, 113, 135-145.

[4] Bouazaoui, L., Perrenot, G., Delmas, Y., & Li, A. (2007). Experimental study of bonded steel concrete composite structures. Journal of Constructional Steel Research, 63(9), 1268-1278.

[5] Kakuma, K., Matsumoto, T., Hayashikawa, T., & He, X. (2011). Fatigue analysis of ECC-steel composite deck under wheel trucking load. Procedia Engineering, 14, 1838-1844.

[6] Luo, Y., Hoki, K., Hayashi, K., & Nakashima, M. (2016). Behavior and strength of headed stud–SFRCC shear connection. I: Experimental study. Journal of Structural Engineering, 142(2), 04015112.

[7] Zhang, S., Shao, X., Cao, J., Cui, J., Hu, J., & Deng, L. (2016). Fatigue performance of a lightweight composite bridge deck with open ribs. Journal of Bridge Engineering, 21(7), 04016039.

[8] Deng, P., Kakuma, K., Mitamura, H., & Matsumoto, T. (2020). Fatigue analysis of partly damaged RC slabs repaired with overlaid UHPFRC. Structural Engineering and Mechanics, 75(1), 19-32.

[9] Graybeal, B. A. (2007). Compressive behavior of ultra-high-performance fiber-reinforced concrete. ACI Materials Journal, 104(2), 146.

[10] Rossi, P., Arca, A., Parant, E., & Fakhri, P. (2005). Bending and compressive behaviours of a new cement composite. Cement and Concrete Research, 35(1), 27-33.

[11] Safdar, M., Matsumoto, T., & Kakuma, K. (2016). Flexural behavior of reinforced concrete beams repaired with ultra-high performance fiber reinforced concrete (UHPFRC). Composite Structures, 157, 448-460.

[12] Nie, J., Xiao, Y., & Chen, L. (2004). Experimental studies on shear strength of steel–concrete composite beams. Journal of Structural Engineering, 130(8), 1206-1213.

[13] Swamy, R., Jones, R., & Bloxham, J. (1987). Structural behaviour of reinforced concrete beams strengthened by epoxy bonded steel plates. Structural Engineer (London. 1924), 65(2), 59-68.
[14] Dieng, L., Marchand, P., Gomes, F., Tessier, C., & Toutlemonde, F. (2013). Use of UHPFRC overlay to reduce stresses in orthotropic steel decks. Journal of Constructional Steel Research, 89, 30-41.
[15] Faella, C., Martinelli, E., & Nigro, E. (2002). Steel and concrete composite beams with flexible shear connection:"exact" analytical expression of the stiffness matrix and applications. Computers & Structures, 80(11), 1001-1009.
[16] Luo, Y., Li, A., & Kang, Z. (2012). Parametric study of bonded steel–concrete composite beams by using finite element analysis. Engineering Structures, 34, 40-51.
[17] De Corte, W., Helincks, P., Boel, V., Klusak, J., Seitl, S., & De Schutter, G. (2017). Generalised fracture mechanics approach to the interfacial failure analysis of a bonded steel-concrete joint. Frattura ed Integrità Strutturale(42), 147-160.
[18] Souici, A., Berthet, J., Li, A., & Rahal, N. (2013). Behaviour of both mechanically connected and bonded steel–concrete composite beams. Engineering Structures, 49, 11-23.
[19] Zhao, G., & Li, A. (2008). Numerical study of a bonded steel and concrete composite beam. Computers & Structures, 86(19-20), 1830-1838.
[20] Miklofsky, H., Brown, M., & Gonsior, M. (1962). Epoxy bending compounds as shear connectors in composite beams. Engineering Research Series, 62-62.
[21] Momayez, A., Ehsani, M., Ramezanianpour, A., & Rajaie, H. (2005). Comparison of methods for evaluating bond strength between concrete substrate and repair materials. Cement and Concrete Research, 35(4), 748-757.
[22] Chmielewska, B., Czarnecki, L., & Krupa, P. (2003). Influence of selected factors on the results of pull-off tests for industrial floors. Paper presented at the 5th International Colloquium-Industrial Floors.
[23] Austin, S., Robins, P., & Pan, Y. (1995). Tensile bond testing of concrete repairs. Materials and Structures, 28(5), 249.
[24] Bonaldo, E., Barros, J. A., & Lourenço, P. B. (2005). Bond characterization between concrete substrate and repairing SFRC using pull-off testing. International Journal of Adhesion and Adhesives, 25(6), 463-474.
[25] J-THIFCOM Construction Association. (2020) The material pamphlet of J-THIFCOM (Japan – Thixotropic Hardening Impermeable Fiber Reinforced Composite). Retrieved from https://www.j-thifcom.com/tech.html.
[26] Beushausen, H., Höhlig, B., & Talotti, M. (2017). The influence of substrate moisture preparation on bond strength of concrete overlays and the microstructure of the OTZ. Cement and Concrete Research, 92, 84-91.
[27] Santos, P. M., & Julio, E. N. (2007). Correlation between concrete-to-concrete bond strength and the roughness of the substrate surface. Construction and Building Materials, 21(8), 1688-1695.
[28] Zanotti, C., Banthia, N., & Plizzari, G. (2014). A study of some factors affecting bond in cementitious fiber reinforced repairs. Cement and Concrete Research, 63, 117-126.
[29] Bentz, D. P., De la Varga, I., Muñoz, J. F., Spragg, R. P., Graybeal, B. A., Hussey, D. S., ... & LaManna, J. M. (2018). Influence of substrate moisture state and roughness on interface microstructure and bond strength: Slant shear vs. pull-off testing. Cement and Concrete Composites, 87, 63-72.

[30] De La Varga, I., Munoz, J. F., Bentz, D. P., Spragg, R., Stutzman, P., & Graybeal, B. (2018). Grout-concrete interface bond performance: Effect of interface moisture on the tensile bond strength and grout microstructure. Construction and Building Materials, 170, 747-756.
[31] Powers, T. C., & Brownyard, T. L. (1946). Studies of the physical properties of hardened Portland cement paste. Paper presented at the Journal Proceedings.
[32] Waller, V. (1999). Relations entre composition des bétons, exothermie en cours de prise et résistance en compression.
[33] Courard, L., Lenaers, J.-F., Michel, F., & Garbacz, A. (2011). Saturation level of the superficial zone of concrete and adhesion of repair systems. Construction and Building Materials, 25(5), 2488-2494.
[34] Huang, W., Kazemi-Kamyab, H., Sun, W., & Scrivener, K. (2017). Effect of cement substitution by limestone on the hydration and microstructural development of ultra-high performance concrete (UHPC). Cement and Concrete Composites, 77, 86-101.
[35] Habel, K., Viviani, M., Denarié, E., & Brühwiler, E. (2006). Development of the mechanical properties of an ultra-high performance fiber reinforced concrete (UHPFRC). Cement and Concrete Research, 36(7), 1362-1370.
[36] Kamen, A. (2006). Time dependent behaviour of ultra high performance fibre reinforced concrete (UHPFRC). Paper presented at the 6th International PhD Symposium in Civil Engineering.
[37] Sprinkel, M. M., & Ozyildirim, C. (2000). Evaluation of high performance concrete overlays placed on Route 60 over Lynnhaven Inlet in Virginia: Virginia Transportation Research Council.
[38] Suthiwarapirak, P., Matsumoto, T., & Kanda, T. (2004). Multiple cracking and fiber bridging characteristics of engineered cementitious composites under fatigue flexure. Journal of materials in civil engineering, 16(5), 433-443.
[39] Suthiwarapirak, P., & Matsumoto, T. (2006). Fatigue analysis of RC slabs and repaired RC slabs based on crack bridging degradation concept. Journal of structural engineering, 132(6), 939-948.
[40] Kakuma, K., Matsumoto, T., Hayashikawa, T., & He, X. (2010). An analytical study on the composite effect of steel deck with ECC overlay reinforcement. Journal of Structural Engineering A, 56, 1282-1291.
[41] Drar, A. A. M., & Matsumoto, T. (2016). Fatigue analysis of RC slabs reinforced with plain bars based on the bridging stress degradation concept. Journal of Advanced Concrete Technology, 14(1), 21-34.
[42] Khan, A. Q., Deng, P., & Matsumoto, T. (2020). Approximate Analytical Conditions of a Panel RC Slab for Reproducing the Fatigue Behaviors of a Real Bridge RC Slab. Journal of Advanced Concrete Technology, 18(1), 1-16.
[43] Matsumoto, T., Wangsiripaisal, K., Hayashikawa, T., & He, X. (2010). Uniaxial tension–compression fatigue behavior and fiber bridging degradation of strain hardening fiber reinforced cementitious composites. International journal of fatigue, 32(11), 1812-1822.
[44] Hobbacher, A. (2016). Recommendations for fatigue design of welded joints and components (Vol. 47). Cham: Springer International Publishing.
[45] Japan Society of Civil Engineers (2013). Steel structure series 22 Steel bridge fatigue countermeasure technology.